

# Improving Mixture Analysis Estimates of Snow-Covered-Area from AVIRIS Data

Thomas H. Painter<sup>1,2</sup>, Dar A. Roberts<sup>1,2</sup>, Robert O. Green<sup>1,2,3</sup> and Jeff Dozier<sup>1,2,4</sup>

<sup>1</sup>Department of Geography, University of California, Santa Barbara

<sup>2</sup>Institute for Computational Earth System Science, University of California, Santa Barbara

<sup>3</sup>Jet Propulsion Laboratory, Pasadena, California

<sup>4</sup>School of Environmental Science and Management, University of California, Santa Barbara

**ABSTRACT** A technique was developed to improve **spectral mixture analysis** estimates of snow-covered-area in alpine regions through the use of multiple snow endmembers. **Snow reflectance** in near infrared wavelengths is sensitive to snow grain size while insensitive in visible wavelengths. **Alpine regions** often exhibit large snow surface grain size gradients due to changes in aspect and elevation. The sensitivity of snow spectral reflectance to grain size translates these grain size gradients into spectral gradients. To spectrally characterize a snow-covered imaged domain with mixture analysis, the variable spectral nature of snow must be accounted for by use of multiple snow endmembers of varying grain size. We perform **numerical simulations** to demonstrate the grain size sensitivity of mixture analysis for a range of sizes and snow fractions. From **Airborne Visible/Infrared Imaging Spectrometer (AVIRIS)** data collected over Mammoth Mountain, CA on April 5, 1994, a suite of snow image endmembers spanning the imaged region's grain size range were extracted. Mixture models with fixed vegetation, rock, and shade were applied with each snow endmember. For each pixel, the snow-fraction estimated by the model with least mixing error (RMS) was chosen to produce an optimal map of sub-pixel snow-covered area. Results were verified with a high spatial resolution aerial photograph demonstrating equivalent accuracy. Fraction under/overflow analysis and residuals analysis confirm mixture analysis sensitivity to grain size gradients.

Address correspondence to Thomas H. Painter, Institute for Computational Earth System Science, 6<sup>th</sup> Floor Ellison, University of California, Santa Barbara, CA 93106. Email: painter@icess.ucsb.edu.

## INTRODUCTION

Snow covers over 30% of the Earth's land surface seasonally and through its melt is the dominant source of fresh water to many regions. An example is the western United States which receives as much as 80% of its annual fresh water from melt of high mountain snow storage. Because snow has the highest albedo of any natural and spatially-extensive surface, it plays an important role in the Earth's radiation budget. The areal

extent of snow cover is likely to be a sensitive indicator of climate change because a warmer climate may force a higher snow line and earlier onset of melt. Thus, it is necessary to monitor snow-covered area and other snow properties at ranges of temporal and spatial scales.

Spatial distributions of snow-covered-area (SCA) are crucial inputs to hydrologic and climatologic modeling of alpine and other seasonally snow-covered areas (Dozier, 1989). SCA is necessary to parameterize energy and hydrology budget calculations in mesoscale and general circulation models (Marshall and Oglesby, 1994), to initialize and validate distributed snowmelt modeling efforts (Harrington et al., 1995), and to provide a basis from which to estimate snow water equivalent (SWE) (Martinec and Rango, 1981). Remote sensing has been shown to be an effective and necessary means of deriving maps of snow-covered-area (Dozier, 1989; Nolin, 1993; Rosenthal, 1993; Rosenthal and Dozier, 1996). Early efforts of mapping snow produced binary classifications through supervised and unsupervised techniques (Rango and Itten, 1976) and thresholds and normalized differences (Dozier, 1989). Yet binary classifications are problematic for areas comprised of combinations of snow, rock, vegetation, water, and ice. To account for this 'mixed pixel' problem, recent efforts in mapping snow-covered-area have used linear spectral mixture analysis to derive sub-pixel snow cover fractions. However, fixed spectral endmember suites have been forced to characterize regions in which rough topography produces snow grain size gradients. Because snow spectral reflectance is sensitive to grain size, grain size gradients represent spectral gradients. In other words, the target (snow) is spectrally manifested as a range of endmembers. Presented here is a technique through which a map of the distribution of surface grain size is incorporated into spectral mixture analysis of AVIRIS data to spectrally characterize the imaged domain and more accurately estimate sub-pixel SCA.

## **BACKGROUND**

### **Snow Optical and Physical Properties**

The spectral signature of snow is characterized by near 100% reflectance in visible wavelengths and moderate reflectance in near-infrared wavelengths. Ice is highly transparent in visible wavelengths, so an increase in grain size has little effect on reflectance. However, in the near-infrared, ice is moderately

absorptive due to an increase of seven orders of magnitude in the imaginary part of the complex index of refraction (Fig. 1). Reflectance, then, is sensitive to grain size, particularly across the wavelength range 1.0 - 1.3  $\mu\text{m}$ , which spans the diagnostic ice absorptions at 1.03  $\mu\text{m}$  and 1.26  $\mu\text{m}$  (Fig. 2). These relationships have been exploited in grain size mapping from remote sensing (Dozier and Marks, 1987; Nolin, 1993; Green and Dozier, 1996). It is important to note that the sensitivity of snow spectral reflectance to grain size decreases with increasing grain size (Fig. 2). Model calculations of spectral reflectance assume a spherical ice crystal. Further reference to grain size in this paper is to the size of this 'equivalent sphere' which is assumed to have the same surface-to-volume ratio as the irregularly shaped grains of the snowpack (Warren, 1982).

Alpine snow-covered regions frequently exhibit large surface grain size gradients, driven largely by altitude, slope, and aspect. When snow is deposited on the surface, grains immediately begin the shape- and size-modifying process of metamorphism. Initially, grain size decreases when fragile, thermodynamically-unstable dendritic crystal branches are destroyed through collisions and water vapor transport. Larger grains then begin to grow at the expense of smaller grains via melt-refreeze and vapor transport driven by microscale and mesoscale temperature gradients (Arons and Colbeck, 1995). Metamorphism is faster at higher temperatures, in the presence of liquid water, and under larger temperature gradients (Langham, 1981; Colbeck, 1979). Therefore, grains tend to be larger at lower elevations, on those slopes oriented to receive maximal incoming shortwave radiation, and in the form of depth hoar at the base of the snowpack and under impermeable ice layers. The rough topography of alpine regions can then result in large grain size gradients, which are translated into spectral gradients by the sensitivity of snow reflectance to grain size.

### **Previous Snow-Covered Area Mapping**

Binary classifications of snow-covered area from remote sensing (Rango and Itten, 1976; Dozier and Marks, 1987; Dozier, 1989) give erroneous results for mixed pixels. To classify a pixel as snow, sub-unity snow fraction thresholds must be met. For example, a pixel composed of, say, 75% areal snow coverage may be classified as snow and, hence, attributed a value of 100% snow cover. This results in an overestimation of SCA. While image-wide errors may offset to produce a reasonable image SCA, the spatial distribution of SCA

is not well represented. This problem grows with the size of the sensor footprint, particularly in rugged alpine terrain. To more accurately map sub-pixel SCA, focus turned to spectral mixture analysis (Nolin, 1993; Rosenthal, 1993).

Spectral mixture analysis has as an objective the definition of sub-pixel proportions of spectral endmembers that may be related to mappable surface constituents (Adams et al., 1993). Linear mixture analysis has been used to map abundance of soil, minerals, and vegetation (Adams et al., 1986; Smith et al., 1990; Roberts, 1991). For cases in which no linear mixture of spectra can adequately represent the measured spectrum, nonlinear mixture analysis has been used (Nash and Conel, 1974; Mertes et al., 1993; Roberts et al., 1993; Borel and Gerstl, 1994). In the linear mixture case, fractions of spectral endmembers determined by least-squares are considered to represent surface areal fractions (i.e. pixel snow fraction). This can be thought of as the 'checkerboard' scenario in which photons interact with only one surface material before interception by the sensor. An example of linear mixing in alpine terrain is rock outcrops surrounded by an optically deep snowpack. In the nonlinear mixture case, fractions of spectral endmembers are disproportionate with surface areal fractions. The disproportional relationship derives from the interaction of photons with multiple surface constituents. Nonlinear mixing in alpine regions occurs when photons are absorbed by snow impurities or the substrate of a shallow snowpack, and through the multiple scattering of photons between vegetation and the snow surface. Details of the equations of mixture analysis will be discussed in a later section.

The linear spectral mixture approach has been shown to be effective in mapping SCA in alpine regions with Thematic Mapper data (Rosenthal, 1993; Rosenthal and Dozier, 1996) and AVIRIS data (Nolin, 1993). These efforts have incorporated fixed endmember suites of snow, vegetation, rock and shade in VIS/NIR bands. However, fixed suites of spectral endmembers are not necessarily optimal for image-wide endmember detectability (Sabol et al., 1992). For snow, the presence of grain size gradients presents a range of snow spectral signatures for which a single snow endmember cannot mathematically account. To explore the discrepancy between theory and the previous application of mixture analysis to mapping sub-pixel SCA, we now summarize the efforts of Nolin (1993) and Rosenthal and Dozier (1996).

In the work by Nolin (1993), when a fixed endmember suite was used on AVIRIS data of Mammoth Mountain, CA, root mean squared (RMS) errors for known snow-covered-areas were reasonable, predominantly in the range of 0 - 3%, and SCA was mapped well. Such a result might imply the adequacy of a single snow endmember in spectrally characterizing the entire spatial domain, yet the associated grain-size map (Fig. 3.8 in Nolin, 1993) reveals near-uniform grain size across above-timberline terrain. Indeed, snow had been falling until 45 minutes prior to image acquisition, at which time cloud cover gave way to clear sky (Nolin, personal communication). In this case, then, a single image snow endmember is valid and adequate. It should be noted though that a comparison of the RMS image (Fig. 2.8 of Nolin, 1993) with the grain size map (Fig. 3.8 of Nolin, 1993) reveals an increase in mixing error with an increase in grain size, from the range 0 - 1% RMS for grain sizes 50 - 75  $\mu\text{m}$  to 2 - 3% for grain sizes of 100 - 125  $\mu\text{m}$ .

To unmix Thematic Mapper data of the Sierra Nevada, Rosenthal and Dozier also used a fixed endmember suite (Rosenthal and Dozier, 1996). However, to account for the spectral difference between sunlit snow and shaded snow, endmembers for both cases were incorporated. In so doing, grain size differences may also have been accounted for. Two reference scenes were used for mixture analysis; a December scene and a May scene. The morning before the December acquisition, 0.36 m of snow had fallen. A large solar zenith angle ( $67^\circ$  at time of overpass) and most likely cold temperatures would have limited grain sizes to a narrow range of fine crystals. A range of snow endmembers would not be necessary in this case. The May acquisition followed 19 days of warm temperatures and smaller solar zenith ( $32^\circ$  at time of overpass) since the last snowfall of 0.05 m. Under these conditions, grain radii grew to 1 mm or larger and the snowpack was isothermal (Rosenthal, personal communication). The sunlit and shaded snow endmembers selected were for coarse-grained old snow. As mentioned before, the sensitivity of the spectral reflectance of snow to grain size decreases as grain size increases. Therefore, grain size gradients in this range of grain sizes would produce little spectral contrast and the use of uniform grain size snow endmembers was effective. RMS error images were not presented, but the scene mean RMS error was 0.012 for both dates.

It is clear from these works that the necessity of multiple snow endmembers of varying grain size can lie

only between snowfall and the complete coarsening of the snowcover. Yet this interim accounts for much of the winter and spring because snowfall resets surface grain size and growth varies spatially. Our working hypothesis then is that multiple snow endmembers which span the grain size range of an imaged domain exhibiting a grain size gradient with radii up to ~1 mm are necessary to spectrally characterize the domain and provide accurate estimates of sub-pixel snow-covered area. We predict that the use of a snow endmember to unmix a pixel of different grain size will result in mixing error and an erroneous snow fraction estimate. In particular, we predict that a snow endmember unmixing a pixel of larger grain size snow will overestimate snow reflectance in the spectral range 1.0 - 1.3  $\mu\text{m}$  and result in negative residuals. Numerical mixture simulations were performed to predict magnitude and sign of error in modeling the mixture spectral signatures and estimating sub-pixel snow fraction. We then tested the hypothesis on AVIRIS data collected over Mammoth Mountain, CA on April 5, 1994.

## SPECTRAL MIXTURE ANALYSIS

The linear mixture assumption was used in this work on the basis of *i*) conclusions by Rosenthal (1993) that linear mixing is broadly applicable for mapping montane snow packs and *ii*) the emphasis of our work was to evaluate the effects of varying grain size on mixture results, which are linear when considered spatially.

Spectral mixture analysis used the following mixing rules (Gillespie et al., 1990):

$$R_c = \sum_{i=1}^N F_i R_{i,c} + E_c \quad (1)$$

where  $R_c$  is the apparent surface reflectance in AVIRIS band  $c$ ,  $F_i$  is the fraction of endmember  $i$ ,  $R_{i,c}$  is the reflectance of endmember  $i$  in AVIRIS band  $c$ .  $N$  is the number of spectral endmembers and  $E_c$  is the residual error in AVIRIS band  $c$  for the fit of the  $N$  endmembers. Fractions are derived using the unconstrained Modified Gram-Schmidt least-squares method (Golub and Van Loan, 1983) in this over-determined case of 224 measurements and  $N$  unknowns where  $N \ll 224$ . Unconstrained analysis requires summation of fractions to unity but permits negative and super-unity fractions for endmembers, whereas constrained analysis forces

fractions to be between 0 and 1 in addition to summation to unity. Constrained analysis limits fractions to physically-meaningful quantities but the added constraint masks sub-optimal mixtures which result in erroneous fractions. The unconstrained method allows mixtures to be optimized which in turn highlights regions of poor modeling.

The residual errors  $E_c$  are calculated by rearranging the linear mixture model:

$$E_c = R_c - \sum_{i=1}^N F_i R_{i,c} \quad (2)$$

Analysis of residuals reveals the spectral locations of errors in modeling the measured spectrum. Residuals have been used to separate and map surface constituents whose spectral signatures are degenerate except for subtle absorption features (Gillespie et al., 1990), such as lignin and cellulose absorptions which separate non-photosynthetic vegetation from soils (Roberts et al., 1993).

The measure of the quality of fit by the mixture model across the spectral range is the average root mean squared (RMS) error, which is calculated as follows:

$$RMS = \left[ M^{-1} \sum_{i=1}^M E_c^2 \right]^{1/2} \quad (3)$$

where  $M$  = number of AVIRIS bands in spectral mixture analysis.

The estimate of sub-pixel snow-covered area is made by calculating the shade-normalized snow fraction estimates, derived as follows:

$$f_s = \frac{F_s}{F_s + F_v + F_r} \quad (4)$$

where  $f_s$  is the shade-normalized snow fraction,  $F_s$  is the spectral snow fraction,  $F_v$  is the spectral vegetation fraction and  $F_r$  is the spectral rock fraction.

## MIXING SIMULATIONS

To confirm the hypothesis and evaluate magnitude and sign of error, we performed linear mixing

simulations for ranges of grain size and snow fraction. Each snow spectrum of grain size from 50 to 1500  $\mu\text{m}$  at 10  $\mu\text{m}$  increments was mixed with a pure quartz spectrum for snow fractions ranging from 0 - 100%. To maintain simplicity, the quartz fraction was treated as complementary in summation of fractions to unity. In excluding a variable shade fraction we treated each pixel as fully-illuminated. Snow spectra were modeled as directional-hemispherical reflectance and the quartz spectrum was acquired from the US Geological Survey Spectral Library contained in Research Systems Incorporated ENVI software. All spectra were converted to 1994 AVIRIS bandpasses. The result was a three dimensional array consisting of 146 snow grain radii by 101 snow fractions by 224 spectral bands.

Mixture analysis, as described above, was performed on the data array with snow endmember of grain radius 200  $\mu\text{m}$ , the quartz endmember used in mixing, and photometric shade (0% reflectance at all wavelengths). The map of RMS error (Fig. 3a) demonstrates that the snow endmember of correct grain radius is necessary to properly model the spectrum, regardless of snow fraction. Independent of snow fraction, RMS error is 0.0% for mixtures with snow of grain size 200  $\mu\text{m}$ . As snow grain size varies from 200  $\mu\text{m}$ , RMS error increases, most quickly at the largest snow fractions. Even at small snow fractions, the mixing error is non-trivial.

Shade-normalized snow fraction (sub-pixel SCA) was calculated from the fractions derived in the mixture analysis. In Figure 3b, we present the shade-normalized snow fractions across snow grain size for the case of 100% snow. At grain radius of 200  $\mu\text{m}$ , shade-normalized snow fraction was properly estimated at 1.0. But, as grain size increases above 200  $\mu\text{m}$ , the predicted sub-pixel SCA increases to nearly 1.2 at 1500  $\mu\text{m}$ . This is because the quartz fraction becomes negative to compensate for the overestimate of reflectance by the 200  $\mu\text{m}$  snow endmember for a larger grain size snow and, hence, the snow fraction is divided by a lesser quantity. Likewise, as grain radius decreases below 200  $\mu\text{m}$ , predicted sub-pixel SCA decreases to 0.86 at 50  $\mu\text{m}$ . This is due to the positive quartz fraction which compensates for the underestimate of reflectance by the 200  $\mu\text{m}$  snow endmember for the smaller grain size snow. In either case, the shade endmember complements the fraction summation to unity. The greater sensitivity of shade-normalized snow fraction to grain size at smaller grain



sizes is due to the aforementioned greater sensitivity of snow reflectance to grain size at smaller grain sizes. While shade-normalized snow fraction errors decrease as snow fraction decreases, they remain non-trivial. This simulation confirms the hypothesis that the proper grain size-snow endmember is required to spectrally characterize and provide an accurate sub-pixel snow fraction estimate for a pixel containing snow.

## DATA and METHODS

This hypothesis was tested on an April 5, 1994 AVIRIS scene of Mammoth Mountain, CA (Fig. 4). The AVIRIS instrument flies aboard the NASA ER-2 at an altitude of 20 km. The nominal instrument field of view is 10.5km and ground instantaneous field of view (GIFOV) is 20m. However, the Mammoth Mountain scene has a mean altitude of approximately 3000m, whereby instrument field of view is ~8.9 km and GIFOV is ~17 m. AVIRIS measures 224 contiguous spectral bands with nominal 10 nm spectral bandwidth, spanning the wavelength range 400 - 2500 nm.

### Site

Mammoth Mountain, CA lies on the eastern slope of the Sierra Nevada at 37°37'45"N, 119°02'05"W (Fig. 4). Imaged elevations range from 2450 m at the town of Mammoth Lakes (far right) to 3362 m at the summit of Mammoth Mountain (just below center of image). North is toward the upper right corner from the center of the image. The summit ridge of Mammoth Mountain is identified as the distinct change in illumination above timberline, down and left of the center of the image. Mean snow water equivalence (SWE) at peak accumulation is 0.8 m at our study site at 2950 m on the north side of Mammoth Mountain. The high mountain mixed forest is dominated by Lodgepole Pine, Mountain Hemlock, White Bark Pine, Red Fir, Jeffrey Pine, and Manzanita. The soils and exposed rock outcrops consist of pumice, glacial till, granite, metamorphic, and recent volcanics.

Solar zenith angle at time of acquisition was 31.4° and azimuth was 1.1° east of south. March 28 through April 3 were characterized by clear skies, maximum temperatures of 5 to 10°C and minimum temperatures of -3.5 to 0.5°C, conditions for rapid grain growth. On the morning of April 4, 6 mm of precipitation fell in the form of snow at the study site. April 5 had clear skies and a high temperature of 5.64°C at the study site.

## Method

Calibrated radiance data was converted to apparent surface reflectance using the atmospheric transmission model MODTRAN3 (Anderson, 1995) linked to a nonlinear least-squares water vapor fitting routine (Green et al., 1993). A map of snow grain size (Fig. 5) was generated using the method of Nolin (1993). The spectral mixture band subset consisted of 175 bands which constitutes the AVIRIS spectrum excluding detector overlapping bands and bands affected by the water vapor absorptions centered at 1.38  $\mu\text{m}$  and 1.87  $\mu\text{m}$ . Previously we used the 4 VIS/ 13 NIR channel selection of Nolin but found results to be too sensitive to noise. Mixing models may be evaluated in three fundamental ways; analysis of RMS error, fraction under/overflow, and residuals (Adams et al., 1993; Gillespie et al., 1990). In this work, optimization was performed by minimizing RMS error. Snow fraction under/overflow and residuals were used to confirm that differences in grain size were responsible for mixing errors.

Image endmembers were chosen for vegetation and rock from regions estimated to be relatively pure using color infrared imagery, complete spectral signatures, and knowledge of the region. The vegetation endmember used in the analysis was extracted from a dense stand of Lodgepole Pine and Jeffrey Pine. Pumice near the summit of Mammoth Mountain was selected as the rock endmember because of its extensive exposure on the mountain. Guided by the grain size map for the scene, five image endmembers were chosen for snow of varying grain size; ~120  $\mu\text{m}$  (N2 SNOW - north side of summit ridge), ~150  $\mu\text{m}$  (SW SNOW - south side of summit ridge), ~253  $\mu\text{m}$  (S SNOW - just above timberline on south side of mountain), ~350  $\mu\text{m}$  (N1 SNOW - just below timberline on ski run on north side of mountain), ~478  $\mu\text{m}$  (E SNOW - below timberline on lobe of eastern-most ski run) (Fig. 5). With vegetation, rock, and photometric shade endmembers fixed, mixture models using the unconstrained Modified Gram-Schmidt method (Golub and Van Loan, 1983) were run with each snow endmember to derive spectral fractions for each constituent. The shade endmember was treated as complementary in endmember fraction summation to unity. RMS error and shade-normalized snow fraction images were produced for each model (Figs. 6,7). Optimization was then carried out by choosing, for each pixel, the lowest RMS error and its respective snow fraction estimate from among the five models to

create a minimum RMS error (MIN RMS) image (Fig. 6) and its accompanying snow fraction image (MIN RMS) (Fig. 7).

## RESULTS/DISCUSSION

### Grain size distribution

The grain size distribution at time of acquisition exhibited large gradients (Fig. 5). Grain radii near the summit were mapped to be in the range of 75 - 175  $\mu\text{m}$  with smaller grains on the north (75-125  $\mu\text{m}$ ). On the south side, grain radii increased from the summit to  $\sim 300$   $\mu\text{m}$  at timberline. On the north side of the mountain, grain radii increased to  $\sim 300$   $\mu\text{m}$  at timberline as well, but continued to increase on the sub-timberline ski runs to  $\sim 600$   $\mu\text{m}$ . Some patches at the base of the mountain approached radii of 700  $\mu\text{m}$ . In this case, multiple snow endmembers should be necessary to properly model the spectral domain and provide accurate estimates of sub-pixel snow-covered area.

### RMS errors

Figure 6 shows RMS error images for each mixing model and the RMS error image for the minimum pixel-by-pixel RMS error among the five models. Inspection of the individual model RMS error images demonstrates that a single snow endmember was inadequate to spectrally model the entire domain. Mean image-wide RMS errors were as follows: 2.24% (N2 SNOW), 1.93% (SW SNOW), 1.22% (S SNOW), 1.13% (N1 SNOW), 1.10% (E SNOW), and 0.82% (MIN RMS).

The N2 SNOW endmember (120 $\mu\text{m}$ ) had near 0% RMS error on the north side of the summit ridge where grain sizes are smallest and small errors of < 2.5% on the south side of the summit ridge where grains are slightly larger. Yet the RMS error increases to 5.0%+ at lower elevations where grain sizes approached 600  $\mu\text{m}$ . The E SNOW endmember (478  $\mu\text{m}$ ), however, gave near 0% RMS error in large-grain domains and errors increasing with decreasing grain size to 5.0%+ RMS error in the small-grain domains. A comparison of the N1 SNOW and S SNOW RMS error results demonstrated that this technique is relatively (not accounting for anisotropy of snow reflectance) insensitive to aspect. Both endmembers were from regions of intermediate

grain size but opposite aspects (different illumination). Nonetheless, spatial RMS error distribution and magnitude were very similar, with differences appearing to be merely due to grain size differences. Likewise, snow fraction estimates for this pair were similar (Fig. 7). Consistent with theory, for both models, RMS increased in regions of larger and smaller grain radii with the largest increases at smaller grain radii. The SW SNOW endmember (150  $\mu\text{m}$ ) also exhibited little mixing error for small grain radii, but increasing mixing error with increasing grain radius. The above patterns are consistent with the hypothesis and the mixing simulations. The RMS error image for MINRMS demonstrated that the suite of snow endmembers was spectrally complementary in reducing image-wide mixing error. The multiple snow endmember approach significantly bounds RMS error and serves to better characterize the spectral domain of this scene. It is important to note that mixing errors for the north side of the summit ridge are consistently smaller than those for the south side of the summit ridge except in the case of the 150  $\mu\text{m}$  endmember model. This is due to illumination: the smaller magnitude of apparent surface reflectance on the north side pixels permits residuals to be smaller in magnitude than for the south side pixels which are well illuminated, even though the error may be larger by percentage.

#### **Sub-pixel snow-covered area**

Shade-normalized snow fractions for individual models and MIN RMS are presented in Figure 7. In individual models, where RMS error was lowest, snow fraction estimates were within reasonable bounds (0.0 - 1.0) and appropriate given location and spectral signature. Where RMS error increased, fraction overflow and/or inappropriate values dominated. Snow fraction estimates for the SW SNOW model (150  $\mu\text{m}$ ) were appropriately near 1.0 at high elevations on the south side of the summit and slightly underestimated at 0.85 on the north side of the summit, yet at low elevations, estimates approached 1.5+ (high RMS error). Snow fraction estimates for the E SNOW model (478  $\mu\text{m}$ ) exhibit near 1.0 values at low elevations, and severe underestimates as low as  $\sim 0.5$  at high elevations. The N1 SNOW and S SNOW models, which are of intermediate grain size ( $\sim 300$   $\mu\text{m}$ ) and similar RMS errors and snow fraction estimates, exhibited snow fractions near 1.0 in middle elevations, overflow ( $\sim 1.3$ ) at low elevations, and underflow ( $\sim 0.6$ ) at high

elevations. The N2 SNOW model (120  $\mu\text{m}$ ) snow fraction estimates were similar to those of the SW snow model, but more appropriate at near 1.0 on the north side of the summit ridge. The snow fraction image for MIN RMS, the desired product, was generally well-bounded and appropriate at all elevations. Above timberline, snow fractions ranged from 75 - 100%. Below timberline on the ski runs, snow fractions were likewise between 80 and 100%. The smaller values were due to the ground instantaneous field of view spanning snow and vegetation. The density and spatial distribution of vegetation was demonstrated by the lower snow fractions in the sub-timberline. While the lower snow fractions in the trees are spectrally appropriate, they simply represent the projection of visible snow into the plane of the instrument. Because snow was most likely hidden below the canopy, the actual fractional snow-covered area was severely underestimated. This is a limitation of optical sensors and not the technique. Geometrical optical modeling combined with imaging spectrometry may eventually have the capacity to solve this problem.

Some scattered pixels were attributed SCA values greater than 1.0 and a large patch at the right edge of the image is attributed negative snow fractions. The patches for which SCA was estimated to be greater than 1.0 corresponded to shaded snow, grain sizes lying between those of endmembers for which the optimal endmember was the smaller, and grain sizes considerably greater than the 478  $\mu\text{m}$  endmember. A more detailed analysis of these errors will be necessary, but it is likely that greater snow endmember grain size resolution, a greater span of snow endmember grain sizes, and the use of shaded snow endmembers will resolve these errors. The large patch of negative SCA corresponded to a south-facing, snow-free slope covered by Manzanita, which is not used as an endmember in this modeling effort. Spectra for Manzanita, acquired with an Analytical Spectral Devices FR field spectrometer, demonstrated that a negative snow spectral fraction would be necessary to model Manzanita with the given pine endmember. More accurate modeling will incorporate multiple vegetation and rock types.

As validation, we compared the MIN RMS sub-pixel SCA estimates with SCA estimates derived from an aerial photograph acquired concurrently with AVIRIS imaging. The aerial photograph was taken by the Wild-Heerbrug RC-10 metric mapping camera which is mounted aboard the ER-2. From 20 km altitude, the

photograph provides spatial resolution of 1.5 - 4 m depending on location within image. The photograph was digitized at greater resolution and coregistered with the MIN RMS sub-pixel SCA map. SCA estimates from the multiple snow endmember mixture analysis and aerial photographs for 13 regions are shown in Fig. 8. The relationship was modeled well by a linear regression (photographic =  $0.0242 + 0.962 \text{ AVIRIS}$ ) with  $r^2 = 0.981$ . 95% confidence intervals are plotted for slope and intercept. The 95% confidence interval for slope was from 0.8723 to 1.0507 and for the intercept was from -0.0301 to 0.0785. Given these bounds, the hypothesis that slope is 1 and intercept is 0 could not be rejected, and we conclude that the technique of multiple snow endmembers gives SCA results comparable to those from high resolution aerial photographs.

### Residuals

Analysis of residuals was used to confirm that grain size difference was the primary source of mixing error. A residual image was created for the SW SNOW (150  $\mu\text{m}$ ) mixture model. The residual image consists of mixing error in each of the 175 spectral bands for the entire spatial domain. We extracted residuals across wavelength for a pure snow pixel with grain size of  $\sim 150 \mu\text{m}$  and the source pixel for the E SNOW 478  $\mu\text{m}$  endmember. As expected, residuals for the similar-sized grain pixel were bounded  $< 0.1\%$ . However, the residuals for the large-grain pixel (478  $\mu\text{m}$ ) were large and grain size-dependent (Fig. 9). Two pairs of strong residuals corresponded to ice absorptions: negative residuals across the 1.03  $\mu\text{m}$  and 1.26  $\mu\text{m}$  ice absorptions and positive residuals across the 1.5  $\mu\text{m}$  and 2.0  $\mu\text{m}$  ice absorptions. The negative residuals were  $\sim 5\%$  and  $\sim 10\%$  respectively, and were due to the overestimation of the large grain reflectance by the small grain endmember. The positive residuals were  $\sim 5.5\%$  and  $\sim 6\%$  respectively, and were due to the dynamic signature of small grain snow in the wavelength range 1.5  $\mu\text{m}$  to 2.5  $\mu\text{m}$  fitting the relatively flat signature of large grain snow (Fig. 2). Reflectances at the 1.5  $\mu\text{m}$  and 2.0  $\mu\text{m}$  absorptions were underestimated while the reflectances at the 1.8  $\mu\text{m}$  and 2.25  $\mu\text{m}$  peaks were overestimated. These results provided the spectral confirmation needed to conclude that grain size mismatch between modeled spectrum and endmember results in mixture modeling errors which increase with the difference in grain sizes.

## CONCLUSIONS

Mixture modeling results for AVIRIS data of Mammoth Mountain, CA demonstrated that multiple snow endmembers representing a range of grain sizes are necessary to spectrally characterize and provide an accurate estimate of snow-covered-area for a scene containing significant snow grain size gradients. Changes in NIR reflectance with grain size were the primary source of mixing error in fixed endmember-suite spectral mixture models. RMS error correlation with grain size in fixed snow endmember models strongly indicated this dependence. Shade-normalized snow fraction estimates for fixed suites of endmembers were accurate in regions for which the snow grain size of the pixel was comparable to that of the snow endmember. But in regions of grain size mismatch, snow fractions were overestimated when the grain size was larger than that of the endmember and underestimated when the grain size was smaller than that of the endmember. Erroneous snow fractions estimates ranged from ~50% to ~150% for nearly pure snow pixels. The optimized sub-pixel SCA map (MINRMS) provided generally well-bounded and appropriate results given location. The small patches of erroneous snow fractions in the optimized map appear to result from inadequate modeling of shaded snow and insufficient resolution and range of grain size of snow endmembers. Residuals analysis provided the spectral confirmation of the mixture analysis grain size sensitivity.

Further work is needed to evaluate the effects of shaded snow, nonlinear mixing in thin/impure snow and between vegetation and snow, anisotropic reflectance from the snow surface, and multiple scattering between terrain facets. In using image endmembers, the number of snow endmembers is limited, whereby the resolution of grain size is coarse. This appears to have caused SCA overflow errors in the optimized map. To improve the resolution of grain size and provide snow endmembers for imaged domains lacking pure snow pixels (e.g. Boreal forest, large-footprint instruments), reference snow endmembers must be incorporated. To account for variation in vegetation and rock type in mapping snow cover, a spectral reference library should be used or the technique of partial-unmixing should be incorporated (Boardman et al., 1995).

Estimates of sub-pixel snow-covered area from the use of multiple snow endmembers provide more accurate parameterizations for hydrologic and climatologic models. AVIRIS-derived SCA results are limited

to use in basins encompassed by the relatively small field of view of the instrument. Nonetheless, AVIRIS data are currently in process of analysis to provide parameterization and validation for distributed snowmelt models of basins such as Emerald Lake, CA (Harrington et al., 1995). The technique of multiple snow endmembers will be useful in deriving global coverage of sub-pixel SCA from data acquired by spaceborne imaging spectrometers such as the TRW LEWIS and instruments with a larger pixel size and field of view, such as the Mission to Planet Earth EOS Moderate Resolution Imaging Spectroradiometer (MODIS).

#### ACKNOWLEDGMENTS

*This work was sponsored under NASA Mission to Planet Earth: EOS grant NAGW-2602 and performed at the University of California, Santa Barbara and the Jet Propulsion Laboratory, Pasadena, CA. We wish to thank Anne W. Nolin for the use of AVIRIS grain size mapping code.*



## REFERENCES

- Arons, E.M., and S.C. Colbeck, (1995), Geometry of heat and mass transfer in dry snow: a review of theory and experiment, *Reviews of Geophysics*, 33(4):463-493.
- Adams, J.B., M.O. Smith, and A.R. Gillespie, (1993), Imaging Spectroscopy: Interpretation Based on Spectral Mixture Analysis, in *Remote Geochemical Analysis: Elemental & Mineralogical Composition*, Pieters and Englert, eds., pp.145-166, Cambridge Univ. Press.
- Anderson, G.P. (1995), "MODTRAN3: An update and recent validations against airborne high resolution interferometer measurements", *Summaries of the Fifth Annual JPL Airborne Earth Science Workshop*, (R.O. Green, ed.), 95-1:5-8.
- Boardman, J.W., F.A. Kruse, and R.O. Green, (1995), Mapping target signatures via partial unmixing of AVIRIS data, *Summaries of the Fifth Annual JPL Airborne Earth Science Workshop*, (R.O. Green, ed.), 95-1:23-26.
- Colbeck, S.C., (1979), Grain clusters in wet snow, *Journal of Colloid Interface Science*, 72(3):371-384.
- Dozier, J., (1989), Remote Sensing of Snow in Visible and Near-Infrared Wavelengths, in *Theory and Applications of Optical Remote Sensing*, (G. Asrar, Ed.), pp. 527-547, Wiley and Sons.
- Dozier, J., and D. Marks, (1987), Snow Mapping and Classification from Landsat Thematic Mapper Data, *Annals of Glaciology* 9:97-103.
- Gillespie, A.R., M.O. Smith, J.B. Adams, S.C. Willis, A.F. Fischer III, and D.E. Sabol, (1990), Interpretation of Residual Images: Spectral Mixture Analysis of AVIRIS Images, Owens Valley, California, in R.O. Green, ed., *Proceedings of the Second Airborne Visible/Infrared Imaging Spectrometer (AVIRIS) Workshop*, JPL Publication 90-54, Jet Propulsion Laboratory, Pasadena, CA, pp. 243-270.
- Golub, G., and C. Van Loan, (1983), *Matrix Computations*, Johns Hopkins Press.
- Green, R.O., J.E. Conel, and D.A. Roberts, (1993), Estimation of Aerosol Optical Depth and Additional Atmospheric Parameters for the Calculation of Apparent Reflectance from Radiance Measured by the Airborne Visible/Infrared Imaging Spectrometer, *Fourth JPL Airborne Geoscience Workshop*, JPL Publication 93-26,v1, Jet Propulsion Laboratory, Pasadena, CA.
- Green, R.O., and J. Dozier, (1996), Inversion for surface snow grain size and liquid water from AVIRIS spectra, *Summaries of the Sixth Annual JPL Airborne Earth Science Workshop, Volume 1. AVIRIS Workshop* (R.O. Green, ed.), (preliminary).
- Harrington, R.F., K. Elder, and R.C. Bales, (1995), Distributed snowmelt modeling using a clustering algorithm, *Biogeochemistry of Seasonally Snow-Covered Catchments*, IAHS Publ. 228, pp. 167-174.
- Langham, E.J., (1981), Physics and Properties of Snowcover, in *Handbook of Snow*, D.M. Gray and D.H. Male, eds., Pergamon Press, pp. 275-337.
- Marshall, S., and R.J. Oglesby, (1994), An improved snow hydrology for GCMs. Part 1: snow cover fraction, albedo, grain size, and age, *Climate Dynamics*, 10:21-37.
- Martinec, J., and A. Rango, (1981), Areal distribution of snow water equivalent evaluated by snow cover monitoring, *Water Resources Research*, 17(5):1480-1488.
- Mertes, L.A.K., M.O. Smith, and J.B. Adams, (1993), Estimating suspended sediment concentrations in surface waters of the Amazon River wetlands from Landsat images, *Remote Sensing of Environment*, 43:281-301.
- Nolin, A.W., (1993), *Radiative Heating in an Alpine Snowpack*, Ph.D. thesis, University of California, Santa Barbara.
- Nolin, A.W., (1993), personal communication.
- Rango, A., and K.I. Itten, (1976), Satellite potentials in snowcover monitoring and runoff prediction, *Nordic Hydrology*, 7:209-230.
- Roberts, D.A., (1991), Separating spectral mixtures of vegetation and soils, Ph.D. dissertation, University of Washington.
- Roberts, D.A., M.O. Smith, J.B. Adams, D.E. Sabol, A.R. Gillespie and S.C. Willis, (1990), Isolating

- Woody Plant Material and Senescent Vegetation from Green Vegetation in AVIRIS data, in Green, R.O., ed., *Proceedings of the Second Airborne Geoscience Workshop: AVIRIS*, Jet Propulsion Laboratory, Pasadena, CA, pp. 42-57.
- Roberts, D.A., M.O. Smith, and J.B. Adams, (1993), Green Vegetation, Non-photosynthetic Vegetation, and Soils in AVIRIS Data, *Remote Sensing of Environment*, 44(2/3):255-269.
- Rosenthal, C.W., (1993), *Mapping Montane Snow Cover at Subpixel Resolution from the Landsat Thematic Mapper*, Master's thesis, University of California, Santa Barbara.
- Rosenthal, C.W., (1995), personal communication.
- Rosenthal, C.W., and J. Dozier, (1996), Automated mapping of montane snow cover at subpixel resolution from the Landsat Thematic Mapper, *Water Resources Research*, 32(1):115-130.
- Sabol, D.E., J.B. Adams and M.O. Smith, (1992), Quantitative Sub-pixel Spectral Detection of Targets in Multispectral Images, *J. Geophys. Res.*, 97:2659-2672.
- Warren, S.G., (1982), Optical Properties of Snow, *Reviews of Geophysics and Space Physics*, 20(1):67-89.
- Wiscombe, W.J., and S.G. Warren, (1981), A Model for the Spectral Albedo of Snow. I: Pure Snow, *J. Atmospheric Sciences*, 37:2712-2733.

## FIGURE CAPTIONS

*Figure 1.* Imaginary part of complex index of refraction of ice.

*Figure 2.* Directional-hemispherical reflectance of snow for illumination angle of  $0^\circ$  and grain radii  $r$  from 50-1000  $\mu\text{m}$ .

*Figure 3.* Numerical mixture simulation results of unmixing with snow endmember of grain size  $r = 200 \mu\text{m}$  and quartz rock endmember, a) RMS error for data array, b) shade-normalized snow fraction estimated by unmixing 100%-snow pixel of given grain size.

*Figure 4.* Reference AVIRIS three-band image of Mammoth Mountain, CA. North is toward the upper right corner from center of image. The summit ridge diagonals across image below and left of center. Ski runs are visible on the north side of the mountain. The town of Mammoth Lakes is seen in the lower right corner. Red = 558.7 nm, Green = 1212.4 nm, Blue = 1678.6 nm. Yellow and bright red are snow-covered, dark red to black are vegetation, and blue is exposed rock, soil, pavement, and shrub-covered soil.

*Figure 5.* Map of optically equivalent snow grain size for Mammoth Mountain, CA, on April 5, 1994, calculated using the technique of Nolin (1993a).

*Figure 6.* RMS error images for individual mixture models and pixel-by-pixel minimum RMS error (MIN RMS). The grain size of the snow endmember used in mixture analysis is displayed with each model.

*Figure 7.* Sub-pixel snow fraction images for individual mixture models and for pixel-by-pixel sub-pixel snow fraction corresponding to model with minimum RMS error (MIN RMS).

*Figure 8.* Photographic versus AVIRIS estimates of sub-pixel SCA for 13 sites. The relationship is modeled well by linear regression with slope of 0.962, intercept of 0.0242, and an  $r^2$  of 0.981. 95% confidence intervals (solid lines) for slope and intercept contain 1 and 0. The accuracies of the methods of estimating sub-pixel SCA are thus considered equal.

*Figure 9.* Spectral plot of residuals for  $\sim 478 \mu\text{m}$  grain size (E SNOW) pure snow pixel unmixed by  $\sim 150 \mu\text{m}$  grain size snow endmember. Large residuals at ice absorptions of wavelength  $\lambda = 1.03 \mu\text{m}$ ,  $1.26 \mu\text{m}$ ,  $1.5 \mu\text{m}$ , and  $2.0 \mu\text{m}$  demonstrate the grain size sensitivity of mixture analysis for snow-covered imaged regions.

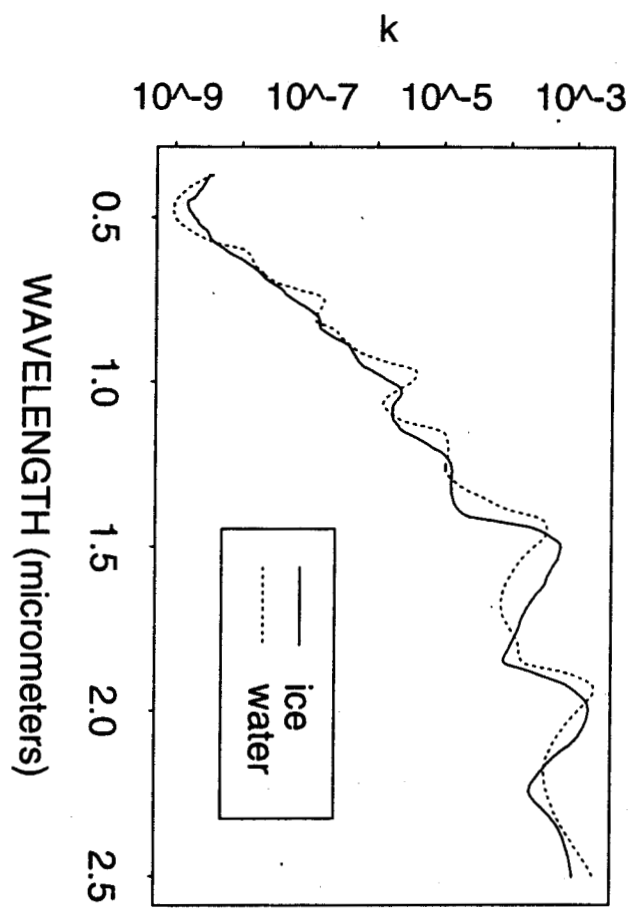


Figure 1

T.H. Painter

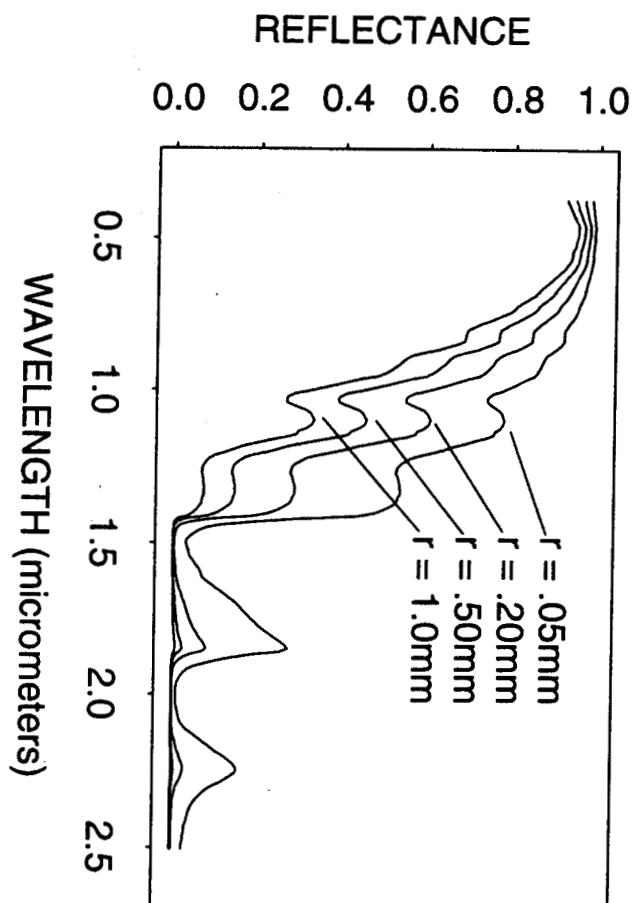


Figure 2

T.H. Painter

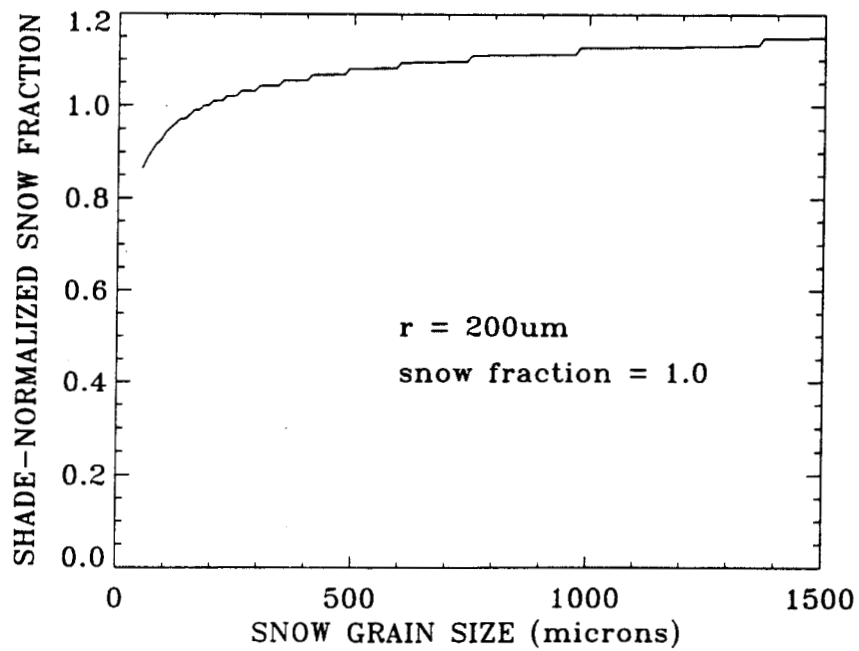
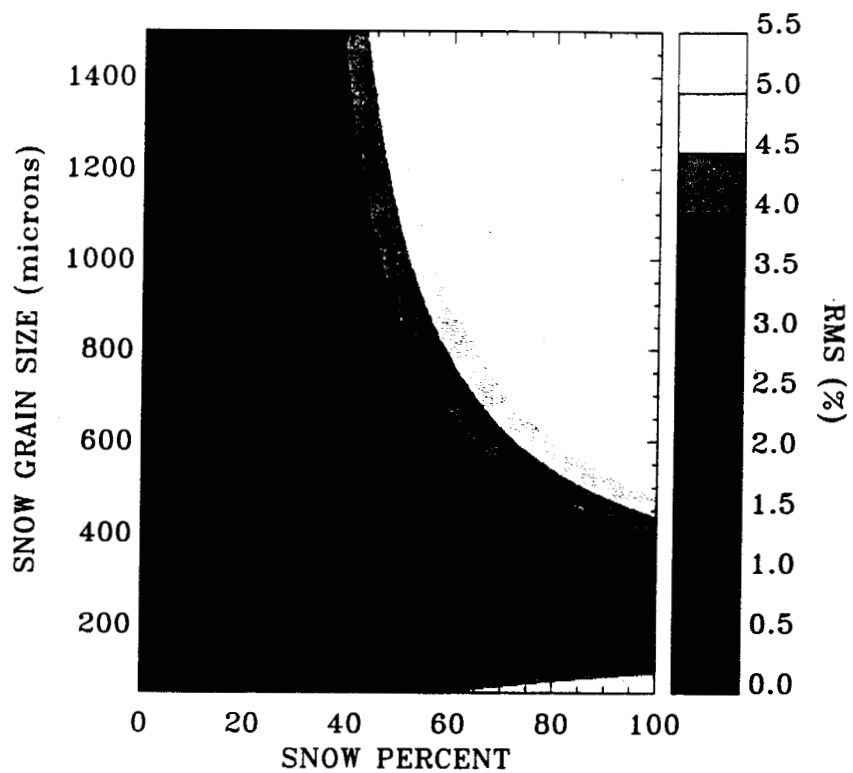


Fig 3

TH Painter

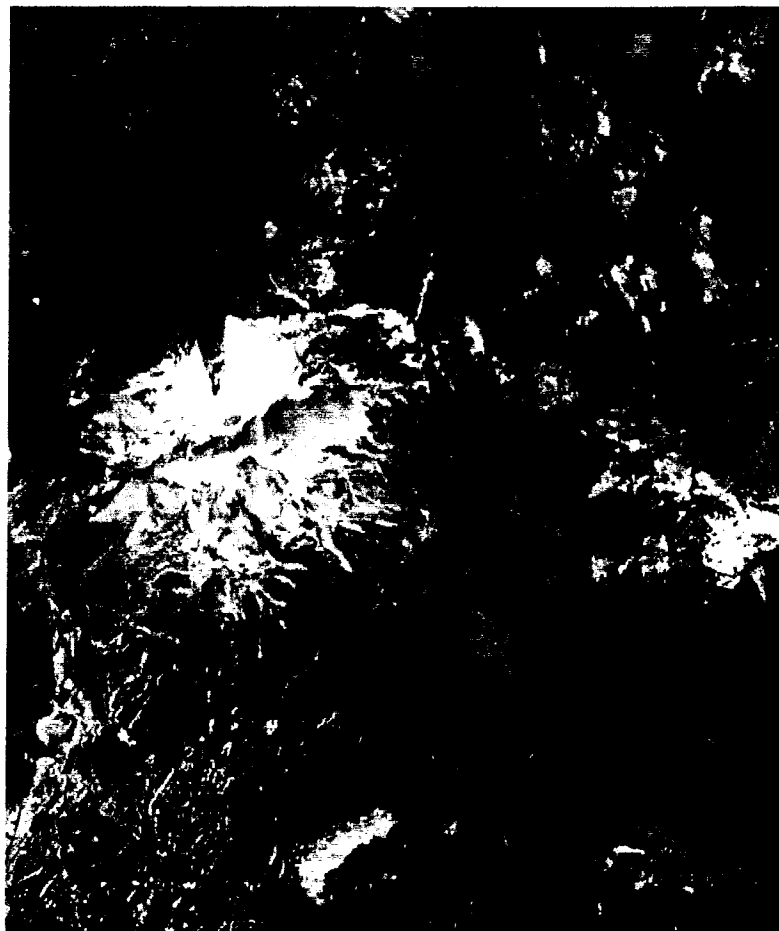
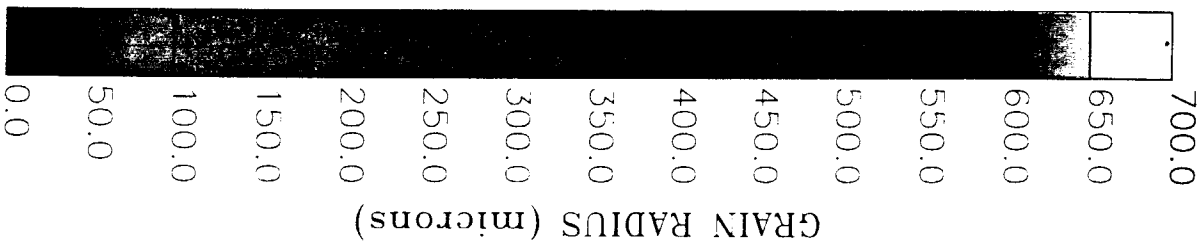
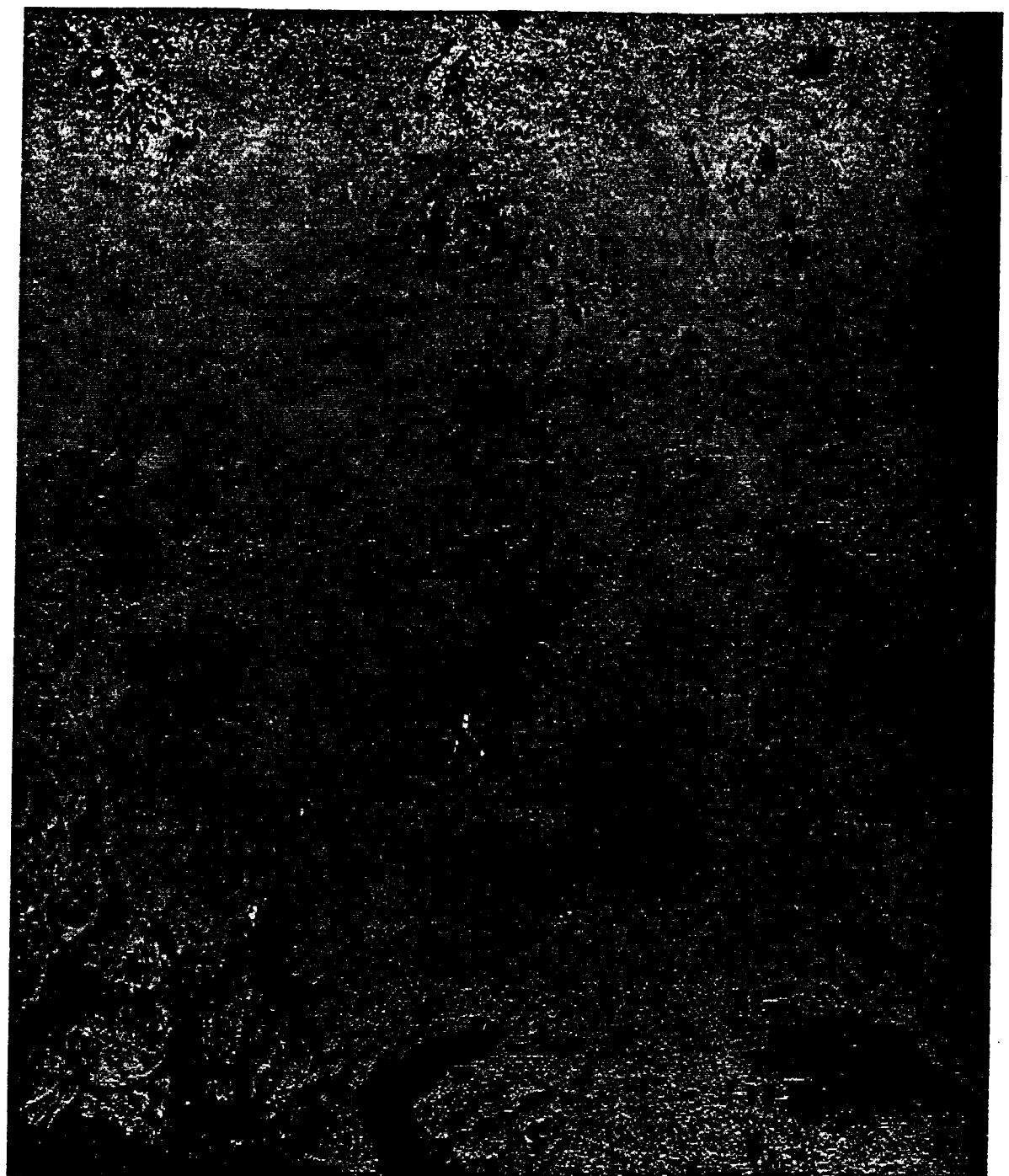


Figure 4

H. Painter

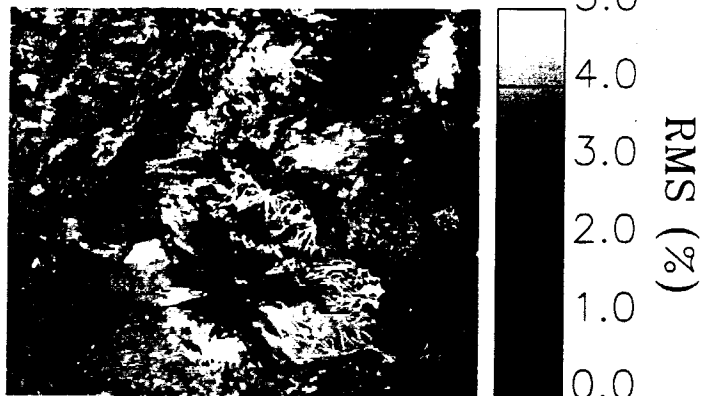


00800000

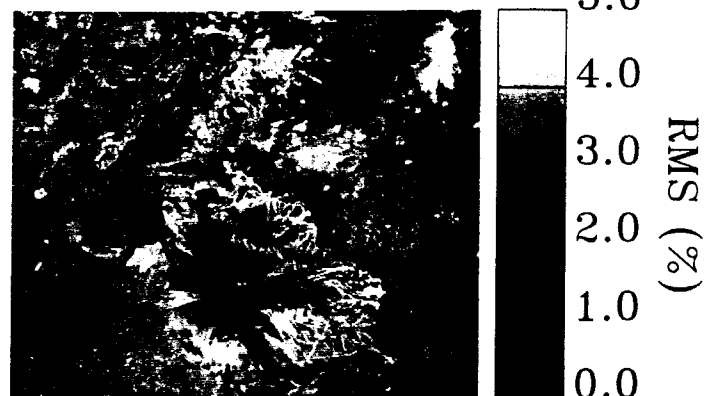
h7



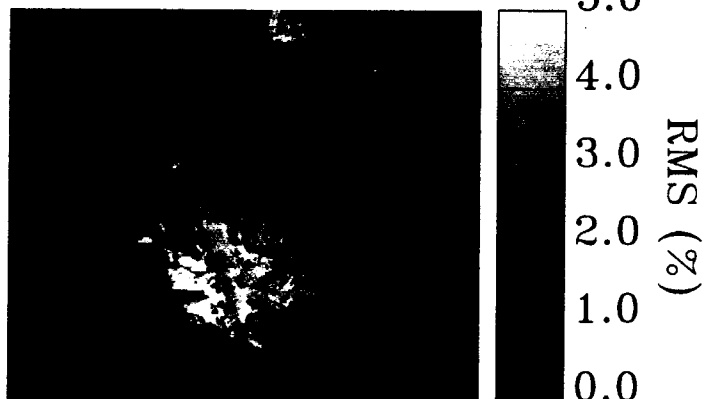
N2 SNOW 120um



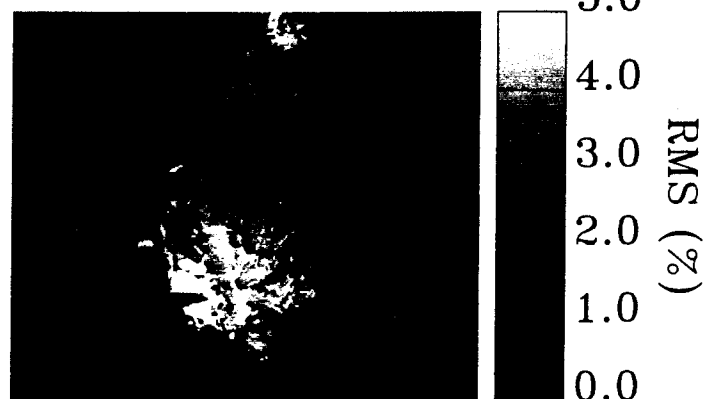
SW SNOW 150um



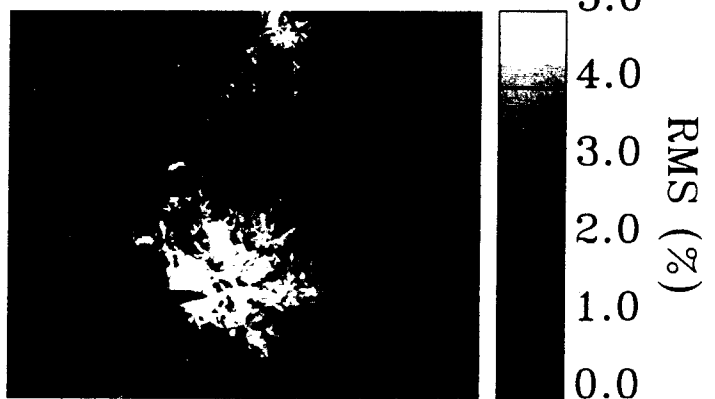
S SNOW 253um



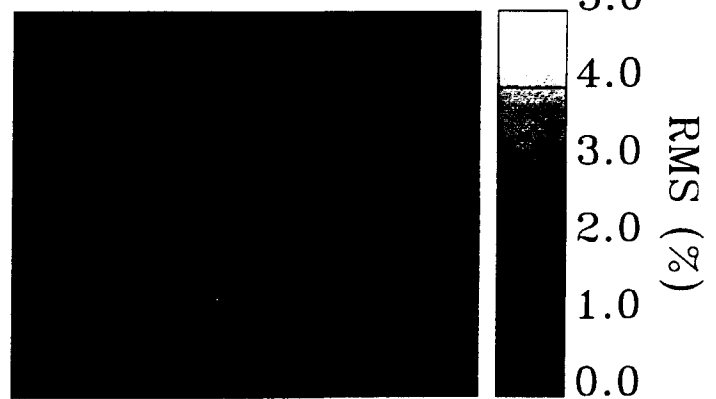
N1 SNOW 350um



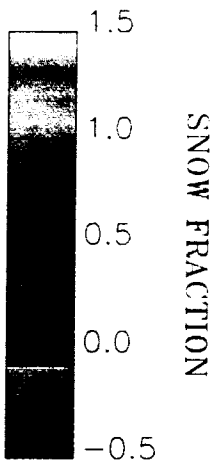
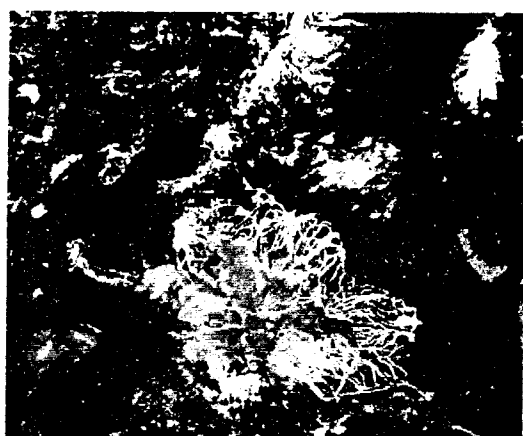
E SNOW 478um



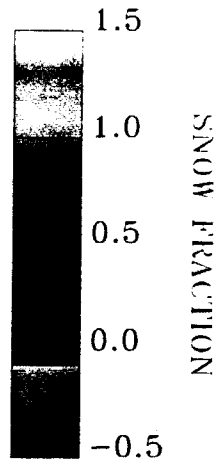
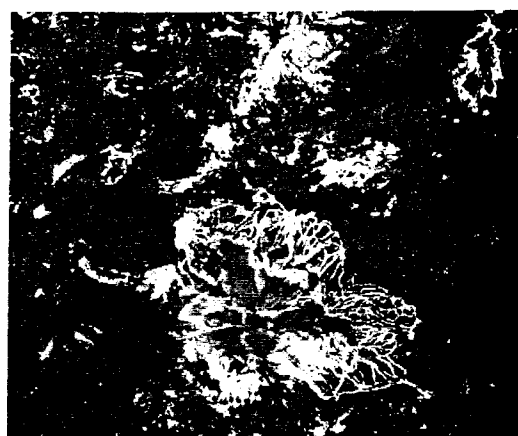
MIN RMS



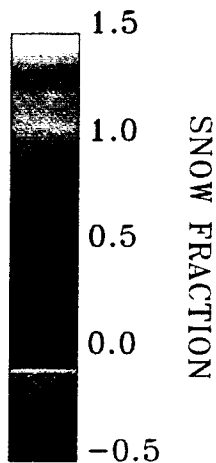
N2 SNOW 120um



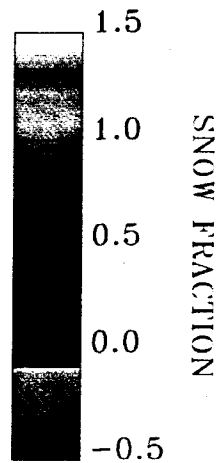
SW SNOW 150um



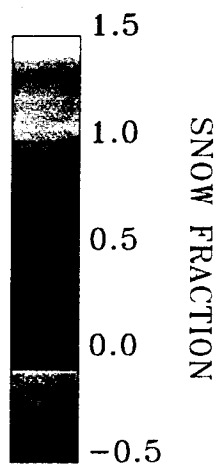
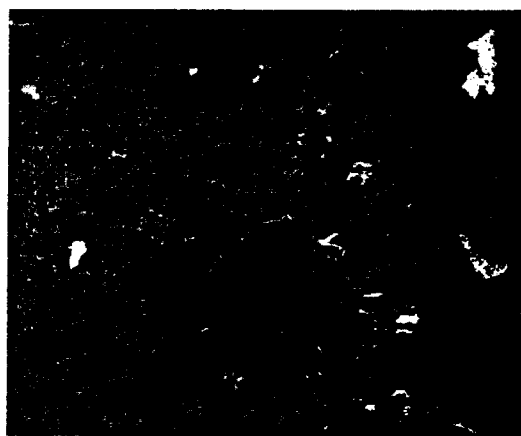
S SNOW 253um



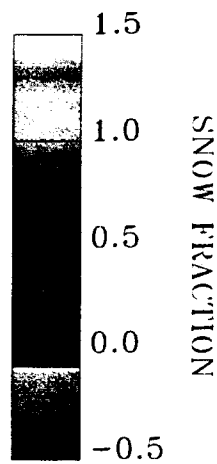
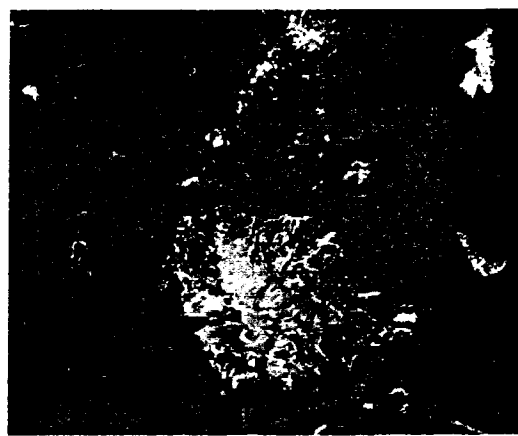
N1 SNOW 350um



E SNOW 478um



MIN RMS



11/18/16

# Photographic versus AVIRIS Estimated Snow Fraction

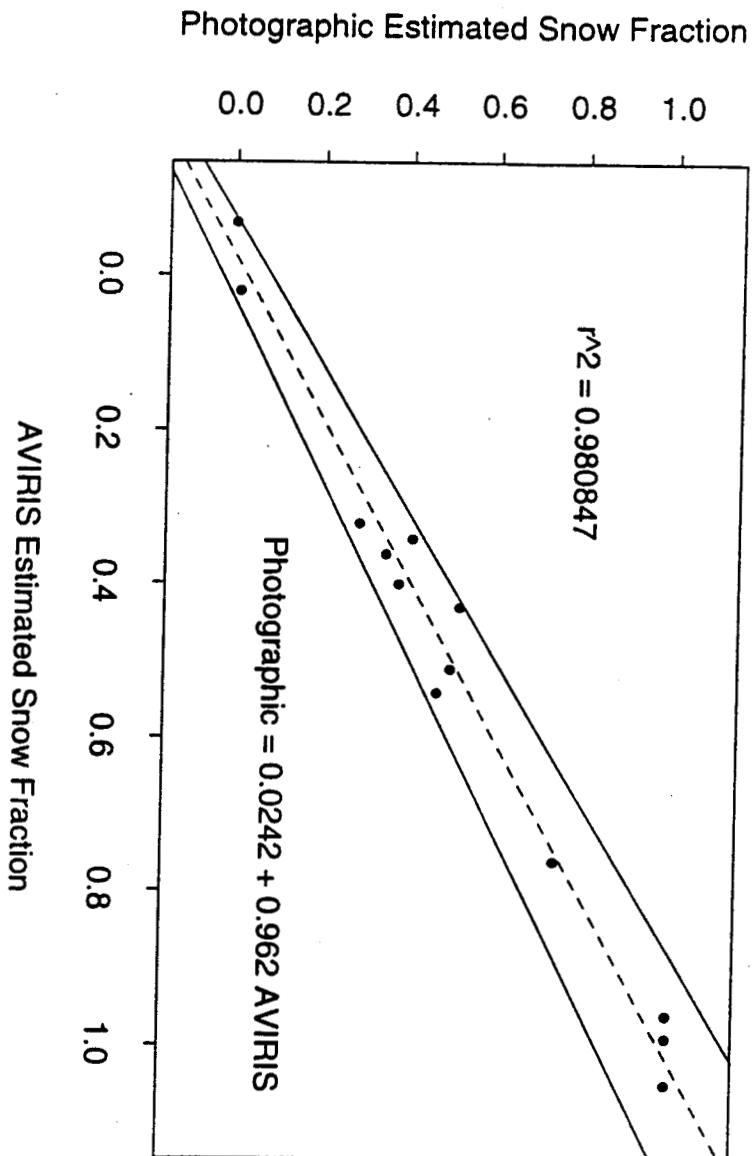


Figure 8

TH Panter

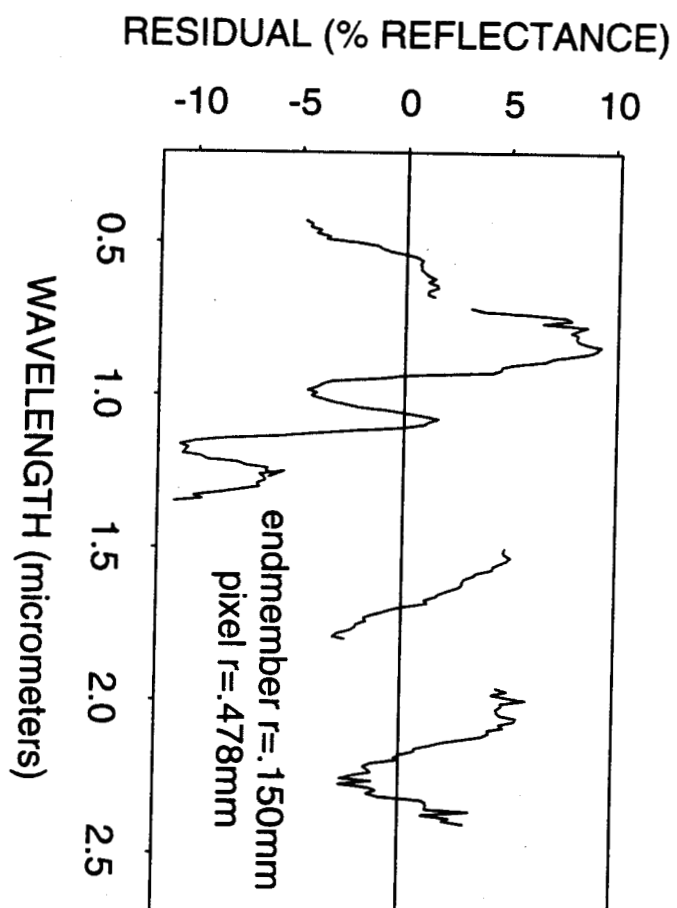


Fig 9

T.H. Painter